# Excitation function shape and neutron spectrum of the $^{7}$Li$(p,n)^{7}$Be reaction near threshold

Guido Martín-Hernández,[1] Pierfrancesco Mastinu,[2] Mario Maggiore,[2] Lorenzo Pranovi,[2] Gianfranco Prete,[2] Javier Praena,[3,4] Roberto Capote-Noy,[5] Fabiana Gramegna,[2] Augusto Lombardi,[2] Luca Maran,[2] Carlo Scian,[2] and Enrico Munaron[2]

[1]*Centro de Aplicaciones Tecnolgicas y Desarrollo Nuclear, 5ta y 30, Playa, La Habana, Cuba*

[2]*INFN - Laboratori Nazionali di Legnaro, Viale dell'Universita 2, 35020 Legnaro, Italy*

[3]*Universidad de Granada, Granada, Spain*

[4]*Centro Nacional de Aceleradores (US-JA-CSIC), Sevilla, Spain*

[5]*NAPC-Nuclear Data Section, International Atomic Energy Agency, A-1400 Vienna, Austria*

(Received 10 March 2015; revised manuscript received 28 June 2016; published 30 September 2016)

The forward-emitted low energy tail of the neutron spectrum generated by the $^{7}$Li$(p,n)^{7}$Be reaction on a thick target at a proton energy of 1893.6 keV was measured by time-of-flight spectroscopy. The measurement was performed at BELINA (Beam Line for Nuclear Astrophysics) of the Laboratori Nazionali di Legnaro. Using the reaction kinematics and the proton on lithium stopping power the shape of the excitation function is calculated from the measured neutron spectrum. Good agreement with two reported measurements was found. Our data, along with the previous measurements, are well reproduced by the Breit-Wigner single-resonance formula for $s$-wave particles. The differential yield of the reaction is calculated and the widely used neutron spectrum at a proton energy of 1912 keV was reproduced. Possible causes regarding part of the 6.5% discrepancy between the $^{197}$Au$(n,\gamma)$ cross section measured at this energy by Ratynski and Kappeler [Phys. Rev. C **37**, 595 (1988)] and the one obtained using the Evaluated Nuclear Data File version B-VII.1 are given.

DOI: 10.1103/PhysRevC.94.034620

## I. INTRODUCTION

The accelerator-based proton-on-lithium reaction is one of the most frequently used sources for producing neutrons in the keV energy range and is used for various applications and cross section measurements. In the latter field, proton energies near threshold are of particular interest since the neutron emission is forwarded, considerably reducing the neutron background. Also the neutron spectrum produced from thick Li or Li compounds targets by protons with energy around 1912 keV resembles the stellar neutron spectrum at a thermal energy of 25 keV [1]. This spectrum has been used in numerous experiments where neutron activation is employed to measure the Maxwellian-averaged cross section of isotopes involved in the slow neutron capture process occurring in the nucleosynthesis of the elements in the universe. In most cases the measurement is performed relative to the $^{197}$Au$(n,\gamma)$ cross section value measured by Ratynski and Kappeler [2].

There is an increasing interest in this technique in order to measure low mass, unstable, and short half-life isotopes driving the creation of more intense neutron sources [3–5]. However there are discrepancies between the $^{197}$Au$(n,\gamma)$ integral cross section measured in Ref. [2] and the value obtained with the time-of-flight technique [6]. This latter measurement is in fair agreement with the Evaluated Nuclear Data File version B-VII.1 (ENDF/B-VII.1). Therefore renewed attention is paid to this reaction and the neutron spectrum was remeasured by two different groups in different facilities [7,8].

We have performed calculations to extend the application of this reaction to astrophysics measurements for different thermal energies. High quality Maxwell-Boltzmann neutron spectra for thermal energies of the distribution ranging from 30 to 50 keV are predicted [9]. This calculation are carried out by computing the differential yield of the reaction for thick targets which is reigned by the reaction kinematics, the stopping power of protons on Li, and the $^{7}$Li$(p,n)^{7}$Be reaction cross section.

There are visible differences between measured cross section data. These differences are shown in Ref. [10]. Model-based spectrum determination considerably differs depending on the cross section used or contradictory results are found when measured neutron spectra are used to derive cross section parameters [11]. In addition to this we have found that the shape of the calculated neutron spectrum is somehow sensitive to the mathematical complications in the solution of the reaction yield. This work primarily intends to measure the shape of the $^{7}$Li$(p,n)^{7}$Be excitation function at near-threshold energies in order to perform accurate calculations of the reaction yield and neutron spectra.

## II. NEAR THRESHOLD $^{7}$Li$(p,n)^{7}$Be REACTION YIELD

The formalism for calculating differential yield in the laboratory system of coordinates for this reaction was reported in Refs. [12,13] and very clearly described by Lee and Zhou [14]. The differential neutron yield can be expressed as

$$\frac{\mathrm{d}^2N}{\mathrm{d}\Omega\,\mathrm{d}E_n}(\theta,E_n) = N_{^{7}\mathrm{Li}}\frac{\mathrm{d}\sigma_{pn}}{\mathrm{d}\Omega'}\frac{\mathrm{d}\Omega'}{\mathrm{d}\Omega}\frac{\mathrm{d}E_p}{\mathrm{d}E_n}\left(\frac{\mathrm{d}E_p}{\mathrm{d}x}\right)^{-1} \quad (1)$$

where $N_{^{7}\mathrm{Li}}$ is the lithium-7 atomic density, $\mathrm{d}\sigma_{pn}/\mathrm{d}\Omega'$ is the center-of-mass differential cross section and $\mathrm{d}E_p/\mathrm{d}x$ is the proton stopping power which is calculated using SRIM 2008 [15]. The Jacobian transformations $\mathrm{d}\Omega'/\mathrm{d}\Omega$ and $\mathrm{d}E_p/\mathrm{d}E_n$ are analytical expressions derived from the reaction kinematics [16] and their product, as a function of the proton

 

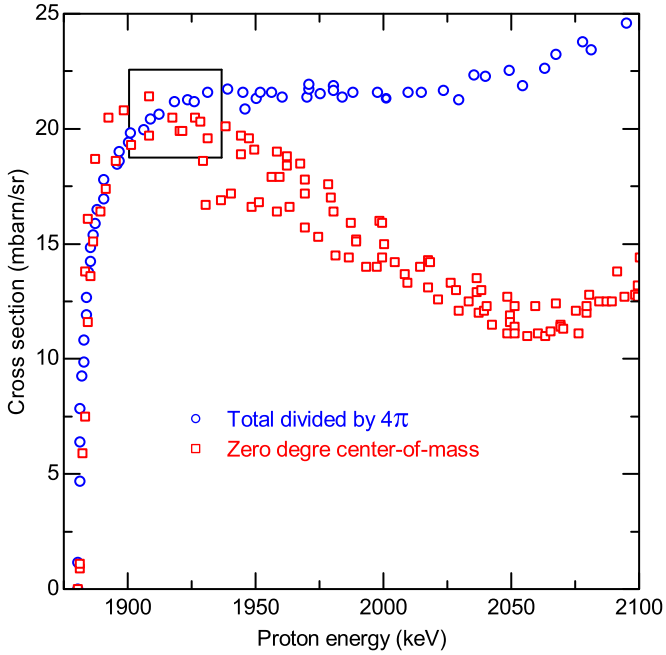


FIG. 1. Laboratory total divided by $4\pi$ (circles) [18] and zero degree center-of-mass (squares) [19] $^{7}$Li$(p,n)^{7}$Be reaction cross sections.

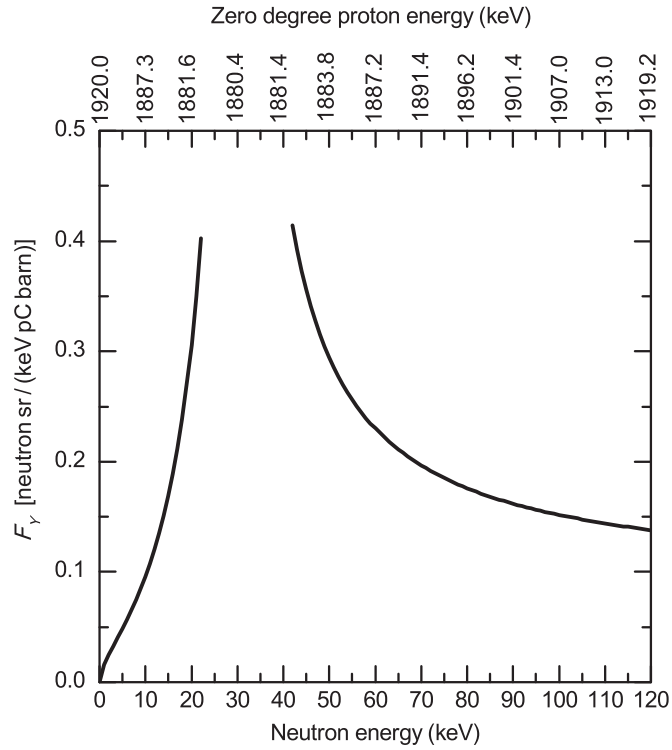


FIG. 2. Yield factor for thick target calculated from Eq. (5) by integrating up to 4° with an incident proton energy of 1920 keV.

energy $E_p$ and the angle of neutron emission $\theta$, has the form

$$\frac{d\Omega'}{d\Omega}\frac{dE_p}{dE_n} = \frac{\pm(m_{Be}+m_n)^2(\cos\theta\pm\zeta)\gamma E_p}{m_p m_n E_p \zeta(\cos\theta\pm\zeta)\pm m_{Be}m_{Li}E_{th}}, \quad (2)$$

where $m_{Li}$, $m_p$, $m_{Be}$, and $m_n$ are the atomic masses of the nuclei taking part in the reaction, $E_{th}$ is the reaction threshold energy, and $\gamma$ and $\zeta$ are parameters having the form

$$\gamma^2 = \frac{m_p m_n}{m_{Be}m_{Li}}\left(\frac{E_p}{E_p - E_{th}}\right) \quad \text{and} \quad \zeta^2 = \gamma^{-2} - \sin^2\theta. \quad (3)$$

At near threshold energies the reaction has been reported to be isotropic in the center-of-mass system [17]. Although there are no accurate data at near threshold energies this can be substantiated by comparing the total cross section data [18] with the differential ones [19].

Figure 1 is a plot of these quantities showing the agreement between both data sets from the reaction threshold $E_{th} =$ 1880.36 keV [20] up to energies inside the square-marked region. In this range the total cross section in the laboratory system is $4\pi$ times the zero degree center-of-mass cross section, confirming the isotropic behavior. The proton energy that limits the isotropic case is around 1920 keV. However, due to the data uncertainties and the energy spacing it is difficult to determine it precisely.

For a proton beam with energy lower than this value the emitted neutron energy spectrum at zero degree in a solid angle with an apex angle equal to $2\theta_{max}$ can be calculated by integrating Eq. (1) over the solid angle. Therefore, the total cross section can be written as

$$\sigma_{pn} = 4\pi\frac{\frac{dN}{dE_n}(E_n)}{F_Y(E_n)}, \quad (4)$$

where

$$F_Y(E_n) = 2\pi N_{^7Li}\int_0^{\theta_{max}}\frac{d\Omega'}{d\Omega}\frac{dE_p}{dE_n}\left(\frac{dE_p}{dx}\right)^{-1}\sin\theta d\theta. \quad (5)$$

The yield factor $F_Y$ for $\theta_{max} = 4°$, the condition met in this experiment, is plotted in Fig. 2. This function shows the double-valued behavior (two neutron energies for a single proton energy) of the neutron energy near the reaction threshold, corresponding to both signs in Eq. (2). Experimentally, when a proton beam slows down in a lithium target from 1920 keV to 1880.36 keV, two tails appear in the neutron spectrum, the high energy tail from high neutron energies down to 29.7 keV, the neutron energy at threshold, and the low energy tail from zero neutron energy up to 29.7 keV.

Close to the reaction threshold $F_Y$ values are neither plotted nor used. When $E_p$ approaches $E_{th}$, Eq. (2) goes to infinity and unreliable results are produced in the calculation at values below $E_p - E_{th} = 1$ keV for $\theta_{max} = 4°$. According to Eq. (4) and using one of the tails of $F_Y$, the shape of the cross section can be calculated from the measured neutron spectrum $dN/dE_n$. This is the concept used in this work. The time-of-flight (TOF) technique was used to measure the neutron spectrum.

## III. EXPERIMENTAL METHOD

### A. Accelerator

The experiment was performed at BELINA, a setup created as part of the 7-MV Van de Graaff accelerator in the Laboratori Nazionali di Legnaro. The purpose of this line is to produce thermal energy-tunable Maxwell-Boltzmann-like neutron spectra with a reduced neutron background for stellar $(n,\gamma)$ cross section measurements. This setup is intended as a test bench for the high flux LENOS facility in preparation at the Laboratori Nazionali di Legnaro [4]. In BELINA, a 3 MHz-pulsed proton beam is injected to the horizontal transport line of the accelerator. In order to reduce the frequency of the proton beam down to 600 kHz, two parallel plates inserted around the midway of the line, are timely biased to sweep off four out of five bursts. This frequency reduction was applied to increase the time, hence energy, resolution by increasing the flight path avoiding overlapping fast neutron signals with low neutron signals from previous pulse. Just before the target, to sense the pass of the proton bunch a capacitive pickup was inserted. The signal induced in the pickup is amplified and digitized, giving the time reference for the TOF measurement. A proton beam current of about 50 nA was used in the experiment.

The measurement was performed at a proton energy of 1893.6 keV. Following calibration of the accelerator energy by means of scanning the $^{7}$Li$(p,n)^{7}$Be reaction threshold, daily proton energy offsets of around 4 keV were observed after shutdown and restart of the machine. Therefore the proton energy was precisely determined using the neutron spectrum (see Sec. V). Measuring the extreme energy of the outgoing particle to determine the energy of the incoming particle in a nuclear reaction has been used in accelerators to determine the beam energy [21,22]. This energy was chosen in order to work far below the limiting energy for the isotropic case in the center-of-mass system to guarantee the applicability of Eq. (4). Also at this energy the production of very low energy neutrons, below 5 keV, is avoided and the neutron background in the room can be observed.

### B. Target

The target is made from pressing a Li foil against a 100 $\mu$m Cu disk. It is mounted on a target holder having all its structure backward from the Li layer with the exception of the target cap which is also a 100 $\mu$m Cu disk. The Li layer is thick enough to reduce the proton energy below the reaction threshold. To avoid oxidation, all operations concerning lithium metal are performed in an argon-filled glove box. The target holder is closed with a gate valve for transport and connection to the beam line without exposing the target to the atmosphere. The target was cooled by flowing water in a circular channel surrounding the target holder.

At the chosen energy, neutrons are emitted in the forward direction within a cone with 70° apex angle where no material, except 200 $\mu$m of Cu, is present.

### C. Detector

The particle detector that triggers the acquisition is located at 690 mm from the target at zero degree respect to the proton beam direction. This distance is measured from the target to the front face of the detector. The detector consists of a neutron-$\gamma$ converter attached to a $\gamma$ detector (see Fig. 3). As neutron-$\gamma$ converter a highly enriched (>99%) $^{10}$B powder, with a density of 1.7 g/cm$^3$, encapsulated in an 8° conical-shaped carbon fiber container is used. The walls of the container are 0.8 mm thick. This $^{10}$B cap is 10 mm width with a 100 mm diameter base and is removable from the detector. In the $^{10}$B$(n,\alpha)^{7}$Li reaction the Li recoil is produced, approximately 94% of the time, in its excited state decaying by the prompt emission of a 478 keV $\gamma$ ray.

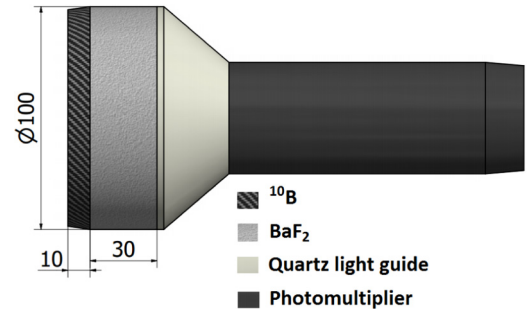


FIG. 3. Schematic of the $^{10}$B -BaF$_2$ detector. Quantities are in millimeters.

The $\gamma$ emission is detected in a 30 mm thickness and 100 mm diameter $BaF_2$ scintillator crystal coupled to a R5113 Hamamatsu photomultiplier tube (PMT) via a quartz light guide using a UV transparent optical coupler fluid. The $BaF_2$ scintillator was chosen because of its fast signal and high efficiency for $\gamma$ radiation. The former is crucial in timing applications. The scintillator, the light guide and the PMT are mounted in a light tight housing. The configuration and materials used in the construction of the detector housing and holding are designed to give sufficient mechanical strength while reducing as much as possible perturbation of the neutron field. Carbon fiber is used for all structural material (detector housing and floor stand) and only light elements with very low mass are in the surrounding of the detector, except for the metal parts of the PMT. According to Monte Carlo simulation of the detector response the presence of the PMT has no effect.

## IV. DATA ANALYSIS

### A. TOF spectrum

The signal outputs from the PMT and the pickup are connected to a DT5751 CAEN digitizer. Proper delay lines are added to adjust the arrival of both signals in the same acquisition window of 1652 ns length with 1 ns per channel. The acquisition is triggered by the detector signal. Digitized signals are transmitted via an optical connection and stored in a computer for offline analysis.

In this experiment, 478 keV photons originate mainly from two sources: the most intense produced in the target by the $^{7}$Li$(p,p'\gamma)$ reaction and those produced in the $^{10}$B cap of the detector by the $^{10}$B$(n,\alpha\gamma)^{7}$Li reaction, the detecting principle of this experiment. Photons from the first reaction arrive to the detector well separated on time from photons

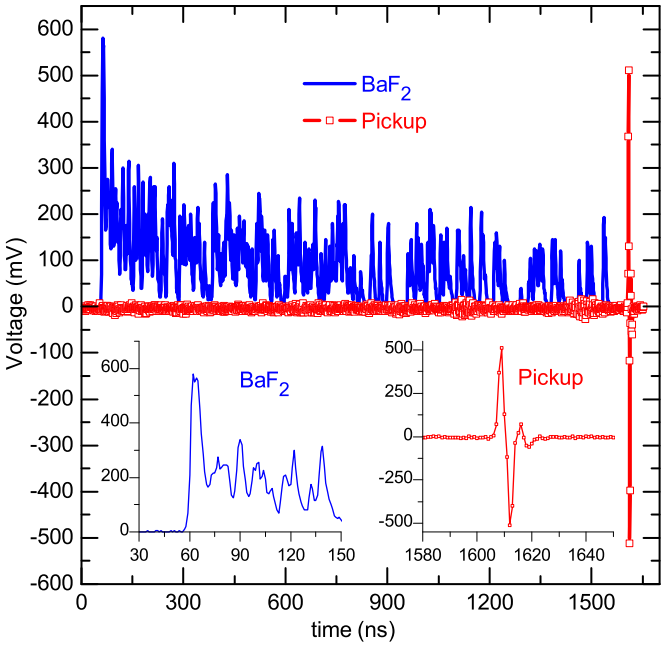


FIG. 4. Typical digitized event composed by two signals, positive from the particle detector ($BaF_2$) and bipolar from beam detector (pickup). This event corresponds to a 478 keV photon from the $^7$Li$(p,p'\gamma)$ reaction ($\gamma$ flash).

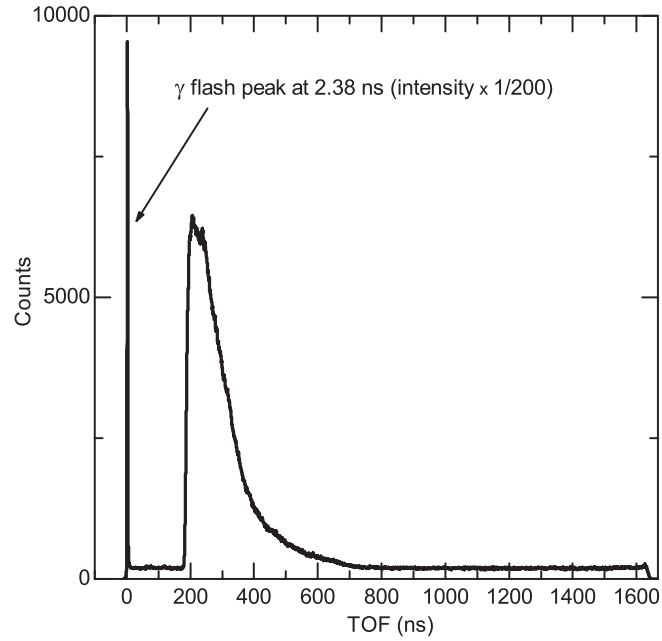


FIG. 5. Measured time-of-flight event distribution with 1 ns bin width. The intensity of the $\gamma$ flash was reduced 200 times.

originated from the second reaction and occupy very few channels corresponding to the gamma flash. The $^7$Be decay, produced in the target during the irradiation, is a third source of 478 keV photons but the intensity of this emission is orders of magnitude lower than the former two and appears as a flat background in the TOF spectrum because it is not time-correlated.

The following algorithm was used to process the detected signals and to produce the TOF spectrum. From the pulse charge spectrum produced at the detector, those events corresponding to 478 keV are selected. The detector was energy-calibrated prior to data analysis. Once the 478 keV event is selected then both signals (detector and pickup) are processed to obtain the time stamp of each. A typical event composed by the two signals is shown in Fig. 4. The fast rise of the $BaF_2$ signal, bottom-left inset of Fig. 4, is used for the time analysis. The negative pulse from the PMT was inverted. A fit to a $A_2 + (A_1 - A_2)/\{1 + \exp[(t - t_0)/\Delta t]\}$ function is performed from the baseline to the maximum voltage, where $A_1, A_2, \Delta t$, and $t_0$ are the fitting parameters. The time $t_0$ corresponds to the time at half-maximum and is used as the trigger time of the event.

For a Gaussian-like proton pulse of few ns width the pickup acts as a differentiator producing a bipolar signal. The zero crossing point of the bipolar signal, bottom-right inset of Fig. 4, is considered the time when the center of mass (charge) of the proton bunch is at the geometrical center of the pickup producing no electric field. In this point the slope of the curve is maximum thus the time uncertainty is minimum. The zero crossing time is calculated by cubic spline interpolation and differentiation of the digitized signal using the values between the maximum and the minimum voltage.

The TOF is then calculated as the difference between the trigger time (particle detector) and the zero crossing time (pickup). A time uncertainty of 200 ps was achieved.

Figure 5 shows the TOF spectrum measured in this work with 1 ns bin width. The time scale is adjusted to have the $\gamma$ flash at 2.38 ns, the traveling time of a photon from the target to about the midplane of the $BaF_2$ crystal. For viewing purposes the intensity of the $\gamma$ flash was reduced 200 times. Considering the high precision of the timing, the time resolution of the experiment is uniquely determined by the time structure of the proton pulse. This pulse has a Gaussian-like shape with FWHM equal to 2.1 ns. This was determined by direct measuring of the bunch signal in a Faraday cup and was confirmed by the $\gamma$ flash structure.

When the $^{10}$B cap was removed a flat background was observed in the entire time spectrum, excluding the $\gamma$ flash peak, showing a time-independent background and no neutron sensitivity of the $BaF_2$ scintillator. The flat background is visible in Fig. 5 between the $\gamma$ flash peak and the neutron region (from around 165 to around 750 ns) and from the latter till the end of the spectrum. No neutrons were observed when the detector was located at angles larger than the neutron cone.

### B. Detected neutron spectrum

When sampling an individual neutron energy there is not a single time-of-flight event but a distribution. This is due to the fact that the detector has a finite size, resulting in a spread in the interaction position and therefore in a spread in the recorded time. Furthermore, neutrons are occasionally elastically scattered before being captured, thus increasing their time of flight. For that reason the TOF spectrum cannot be directly converted into an energy spectrum using the time to energy relation.

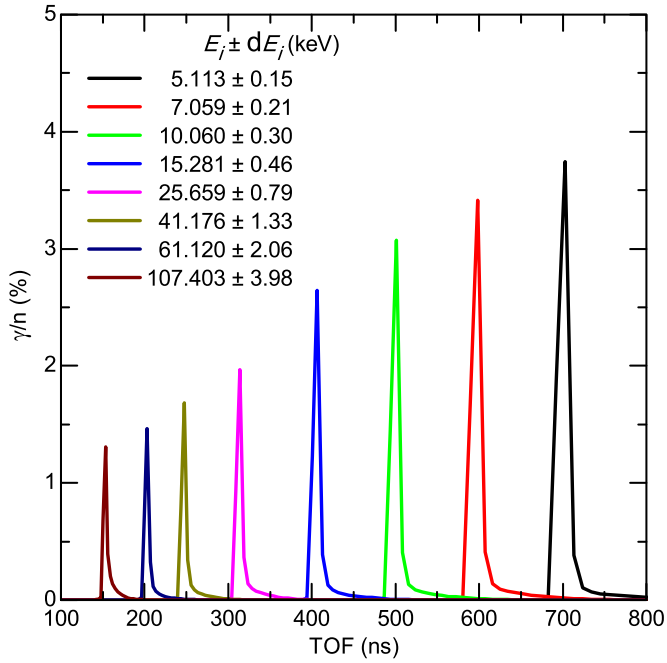


FIG. 6. Calculated time distribution of some neutron energy groups, with $E_i \pm dE_i$ energy widths. Shorter times correspond to higher energies.

In the TOF spectrum, the score $S_j$ for the $j$th time bin is composed by tallying the components of the detected energy spectrum $N_i^{\text{detected}}$ times a factor equal to the contribution of the $i$th energy interval to the $j$th time bin. This factor is the corresponding element $RM_{ij}$ of the detector response matrix, $\mathcal{RM}$. The solution of the system of $n$ equation formed by

$$S_j = \sum_{i=1}^{n} N_i^{\text{detected}} RM_{ij} \quad j = 1 \ldots n, \tag{6}$$

where

$$\sum_{i=1}^{n} RM_{ij} = 1 \tag{7}$$

provides the detected neutron spectrum.

$\mathcal{RM}$, was determined using Monte Carlo simulation. Neutrons with energies $E_i \pm dE_i$, where $dE_i$ is given by the energy uncertainty of the setup, were allowed to strike the detector and the time distribution of the events was determined. The MCNP [23] code was used for this purpose. Neutrons are emitted from a circular surface of 2 mm diameter, resembling the beam spot. The emission occurs within a cone with 8° apex angle, corresponding to the solid angle formed by the source and the detector. In order to mimic the beam time structure, the source is sampled as a Gaussian-shaped time-dependent distribution with FWHM = 2.1 ns. When a 478 keV photon produces a full-energy deposition interaction in the $BaF_2$ crystal the event is time-scored.

$\mathcal{RM}$ is almost diagonal having a symmetric time spread and a small tail toward higher times due to multiple interaction events. Figure 6 shows a plot of some columns of $\mathcal{RM}$, before applying the normalization condition of Eq. (7). Around 5 to 8% of the detected signals are due to backscattered neutrons from the $BaF_2$ and they appear on the tail of each distribution. This effect has little impact on the time resolution of the detecting system modifying it in less than 0.5%.

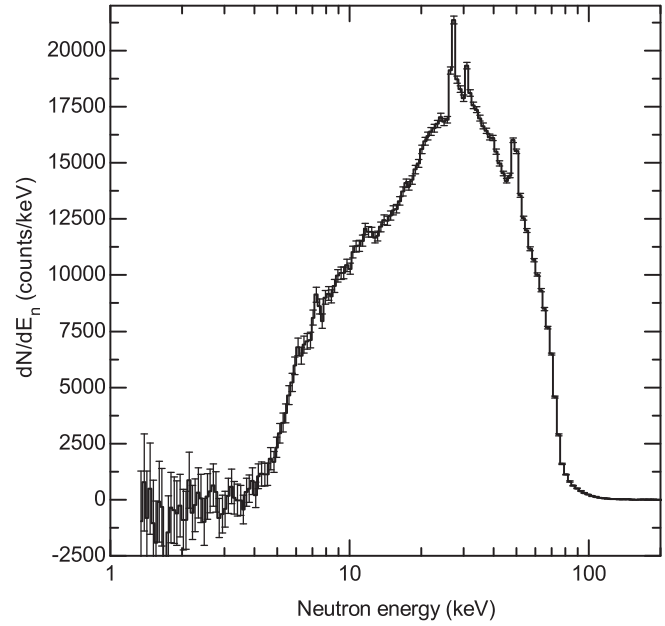


FIG. 7. Detected neutron spectrum. Uncertainties are due to the counting statistics.

Figure 7 shows the detected neutron spectrum obtained from solving the system of Eqs. (6). The plotted uncertainties are due to counting statistics. The uncertainties resulting from the Monte Carlo calculation of $\mathcal{RM}$ are negligible because only the kinematics of the neutron elastic scattering (nuclear masses) and the geometry and composition of the detector are involved. The uncertainty of the reaction cross sections involved in the detection process is considered in the efficiency calculation and is reported in Sec. IV C.

The energy bins of this spectrum are equal to twice the energy uncertainty. The non-relativistic equation for the energy determination was used, producing an energy uncertainty $\sigma E_n = 2E_n\sqrt{(\delta L/L)^2 + (\delta t/t)^2}$, where $\delta L = 0.005$ m and $\delta t = 0.89$ ns. While the flight path is fixed the TOF is not, therefore a nonlinear binning of the energy spectrum is obtained with energy resolution $(2.35\frac{\sigma E_n}{E_n}100)$ ranging from 3.4% at 3 keV to 4.3% at 100 keV.

Some structures appear in the detected neutron spectrum at 7.3, 27.3, 30.9, and 49.2 keV. These structures are due to backscattered neutrons from the $BaF_2$ crystal where the last three belong to wide resonances in the scattering cross section of $^{19}$F and the first to a combination of a resonance in $^{136}$Ba with a dip in $^{138}$Ba.

### C. Detection efficiency

In order to convert the detected neutron spectrum into the emitted by the source (measured), the detection efficiency must be calculated. The cross section of the $^{10}B(n,\alpha\gamma)^7Li$ reaction is used as a standard from thermal energies to 250 keV [24].

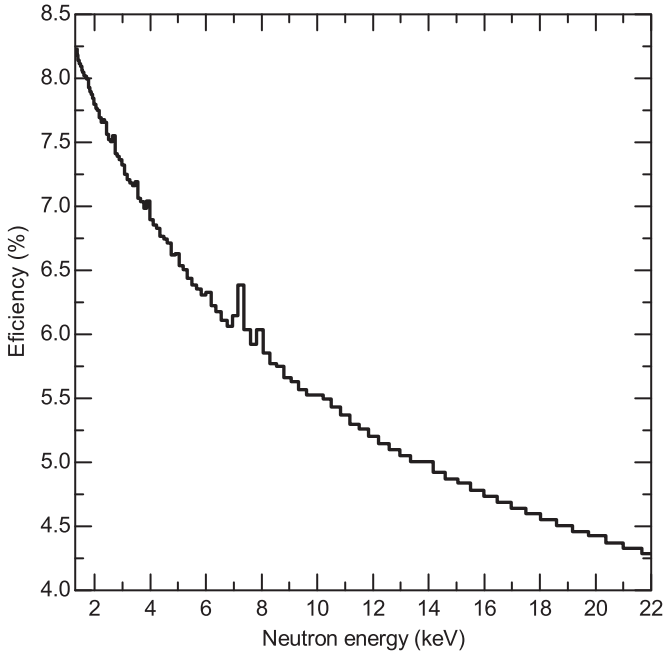


FIG. 8. Calculated neutron detection efficiency. Uncertainties vary from 1% at 2 keV to 2% at 22 keV.

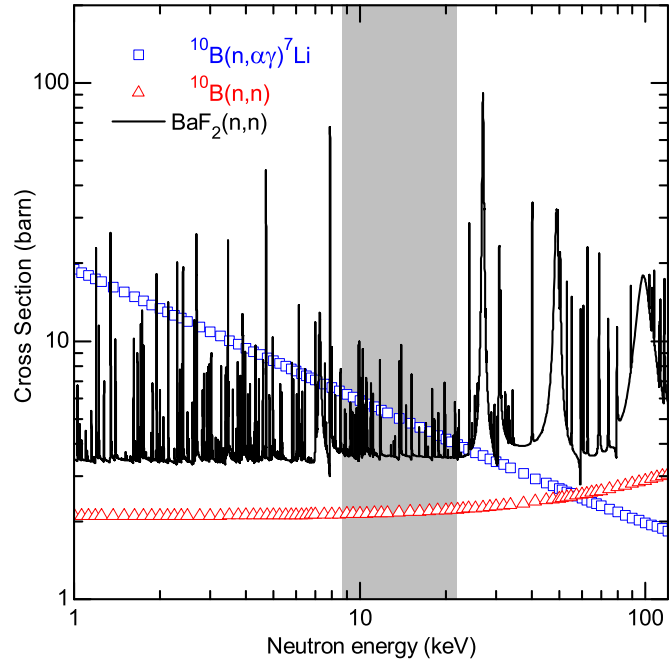


FIG. 9. Reaction cross sections involved in the detection process taken from ENDF/B-VII.1 [27] .

In the energy interval comprising this study ranging from 1 to around 100 keV this cross section is known with an uncertainty between 0.09 and 0.4%.

Using this reaction as detecting principle will produce very precise results because the major source of uncertainty in this type of experiment is the detection efficiency. To satisfy this condition the influence of the remaining reactions, whose cross sections are not known with such precision, must be reduced as much as possible. The neutron detection efficiency for each energy group in the energy range from 2 to 22 keV was calculated by integrating its time distribution (see Fig. 6). This function is plotted in Fig. 8.

It is more advantageous to use the low energy tail of the neutron spectrum to calculate the cross section $\sigma_{pn}$ than to use the high energy tail. This can be supported from the cross section analysis of the main reactions entering into play in the neutron interaction process. These reaction cross sections are represented in Fig. 9. Concerning the reactions on $^{10}$B, the direct $(n,\alpha\gamma)$ reaction is more probable than the combined $(n,n)$–$(n,\alpha\gamma)$ in the lower energy part. The combined process adds uncertainty to the detection efficiency because the 2% uncertainty of the $(n,n)$ reaction cross section is higher than the $(n,\alpha\gamma)$ one. In the high energy tail the combined reaction is more likely, thus the uncertainty is bigger.

The presence of the $BaF_2$ scintillator produces a modification to the detector response due to the subsequent detection of backscattered neutrons. In this case the difference between the high and the low energy tails is more marked due to the existence of wide resonances in the former region with uncertainties ranging from 15 to 50%. In contrast, in the low energy region (grey marked in Fig. 9) the cross section is flat (excluding sharp resonances from barium which have no influence due to the experimental energy resolution) having no effect in the shape of the efficiency, only on its absolute value. A 15% uncertainty for the $BaF_2$ elastic scattering cross section was chosen in this region. Considering the reactions involved in the detection process, their contribution as calculated from the simulation and the described uncertainties, the uncertainty on neutron detection efficiency from 2 up to 22 keV varies from 1 to 2%.

## V. RESULTS

Figure 10 shows the measured (open square with error bars) low energy tail of the emitted neutron spectrum at $0 \pm 4^\circ$ with respect to the proton beam direction, from the $^7$Li$(p,n)^7$Be reaction produced by a proton beam with $E_p = 1893.6$ keV impinging on a thick lithium target. The spectrum is obtained by correcting the detected neutron spectrum (Fig. 7) with the calculated detection efficiency (Fig. 8). The error bars embody both statistical as well as systematic uncertainties. The absence of neutron background due to room (floor) neutron-scattering is visible below around 3.5 keV. It is also visible a bump at around $E_n = 12$ keV. Great care has been taken in the construction of the detector and its housing and holding to avoid the presence of materials with sharp structures in the cross section. The origin of this deviation is unknown to us but it does not affect, within the quoted uncertainty, the shape of the reaction cross section which is calculated next.

Relative values of $\sigma_{pn}$ are calculated using Eq. (4) at proton energies corresponding to the neutron energy points measured in the energy spectrum from around 8 to 22 keV. Figure 11 shows these values where they are plotted together with previous measurements. Proton energies are calculated from neutron energies using the reaction kinematics.

There are three available measurements of the reaction cross section near threshold [18,25,26]. The data of Sekharan *et al.* are in visible disagreement with the remaining therefore they

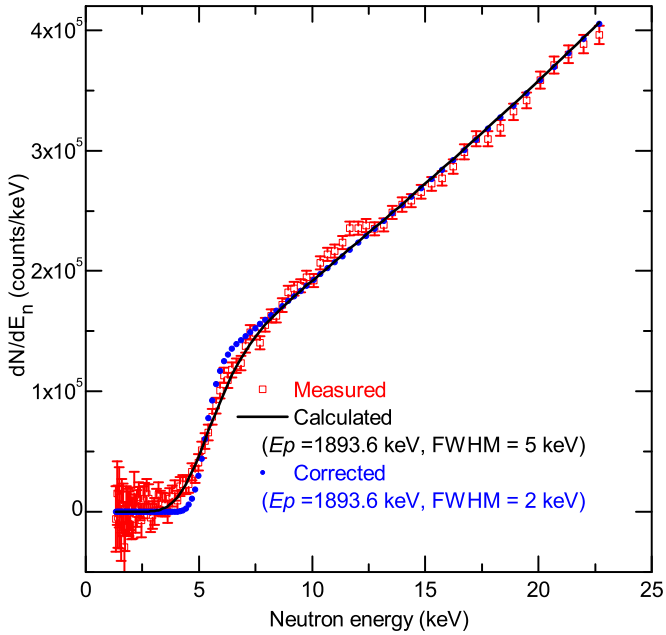


FIG. 10. Measured (open square with error bars) low energy tail of the neutron spectrum emitted at $0 \pm 4^\circ$ by the $^7$Li$(p,n)^7$Be reaction induced in a thick target by a proton beam with $E_p = 1893.6$ keV (open square with error bars). Calculated (solid line) as well as neutron energy broadening corrected (solid circles) spectra are also plotted.

were excluded from the analysis. The data of Newson *et al.* (taken from Fig. 2 of Ref. [25]) were scaled up 8.5% to match the integral value of Macklin and Gibbons. The data of Macklin and Gibbons and Newson *et al.* are shifted in the energy scale in about 0.5 keV to correct for the currently known value of the reaction threshold. The values of $\sigma_{pn}$ calculated in this work are normilized to Macklin and Gibbons and Newson data. Absolute determination of $\sigma_{pn}$ was not possible due to the lack of reliable proton beam current indication. A good agreement between the data is observable validating the reliability of our measurement. As suggested in Ref. [25], the shape of the cross section near threshold can be reproduced by the Breit-Wigner single-resonance formula reduced to

$$\sigma_{pn} = \frac{AC\sqrt{1-\frac{E_{\rm th}}{E_p}}}{E_p\left(1+C\sqrt{1-\frac{E_{\rm th}}{E_p}}\right)^2}. \quad (8)$$

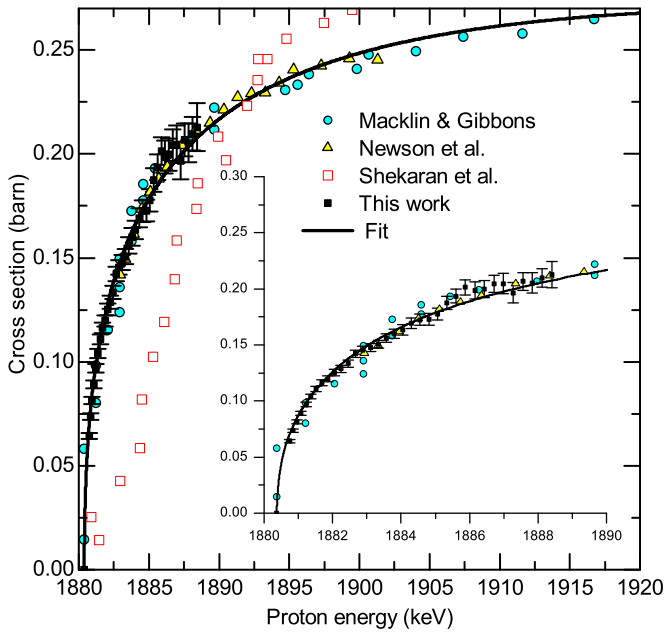


FIG. 11. $^7$Li$(p,n)^7$Be reaction cross section derived from the energy spectrum (close square with error bars) normalized to Macklin and Gibbons [18] and to Newson *et al.* [25] scaled to Macklin and Gibbons. Sekharan *et al.* [26] data are also plotted. The solid line represents the best fit to all data using Eq. (8).

The fit performed using the three data sets from threshold to 1920 keV gives the following fitting parameters: $A = 168 \pm 3$ b keV/sr and $C = 5.0 \pm 0.2$. The relative uncertainties in our cross section data are due to the uncertainties in the determination of the neutron spectrum. $F_Y$ uncertainty can be neglected because this magnitude depends on nuclear masses and proton on lithium stopping power. The value of the latter is known within a 3% and influences $F_Y$ by less than 1% in the energy range of this measurement.

With the knowledge of the shape of the excitation function and integrating Eq. (1) over the emission angle, neutron spectra can be calculated for a particular proton energy spectrum using a computer code. Additionally we introduce a minimization procedure in the code where a Gaussian-shaped proton beam impinges the target with unknown energy $E_p$ and energy spread FWHM, consequently determining these values for a measured neutron spectrum.

At first, we reproduced the low energy tail measured in this work. The rapid drop to zero at the beginning of the low energy tail of the neutron energy spectrum is a very precise indicator of the effective proton energy entering in the Li layer which is in general at the end of an experiment, a bit lower than the energy indicated by the accelerator. The effective proton energy decreases during experiments, due to material deposition on the target surface. The material is usually carbon, present in the vacuum pumps of the system and in some parts of the accelerator.

The low energy tail of the measured neutron spectrum was best reproduced with a proton energy of $1893.6 \pm 0.2$ keV and an energy spread of 5 keV represented as calculated (solid line) in Fig. 10. This simulated neutron energy spread is composed of the real energy spread of the proton beam and a neutron energy straggling introduced by the detector finite size and material composition, usually called energy resolution function. The proton beam energy spread was determined by measuring the proton beam distribution by time-of-flight and was equal to 2 keV. Consequently the actual neutron spectrum hitting the detector has a sharper fall and is plotted in Fig. 10 as corrected neutron spectrum (close circles). When simulated by MCNP the interaction of the neutron spectrum calculated with the code for a proton beam at $E_p = 1893.6$ keV and an energy spread of 2 keV, the resulting neutron spectrum has a broad fall alike to the experimental one.

Such broadening effect is larger at higher neutron energies. This result along with a higher uncertainty on the determination of the detector efficiency produce a larger indetermination in the calculated proton energy. Nevertheless, the fall of the high energy tail can also be used to calculate the proton energy impinging the target. In our case this values is equal to $1892.5 \pm 2.1$ keV, just differing with the former determination in 0.05%.

## VI. IMPLICATIONS

A comparison with recent measurements of the neutron spectrum produced at $E_p = 1912$ keV on thick Li or LiF targets taken at $0 \pm 3^\circ$ with respect to the proton beam direction was performed. Figure 12 shows these spectra and the one calculated in this work for a proton beam with an energy spread of 3.5 keV (FWHM). Spectra from literature, referenced as Feinberg *et al.* taken from Ref. [10] and Lederer *et al.* taken from Ref. [7] were rebinned to 1 keV energy step and are normalized to unit area from 3 to 85 keV.

The left grey-marked region represents the measured values in this work while the one on the right is calculated from the reaction kinematics based on the values measured in the left region. The remaining regions are based on extrapolation to Macklin and Gibbons and Newson *et al.* data. The relative differences were calculated as $(Y_{\text{cal}} - Y_{\text{exp}})/Y_{\text{cal}}100$. In general there is a fair agreement with relative differences fluctuating between the reported uncertainties, except the extreme parts of the spectra. Nevertheless a tendency of miscounting neutrons with increasing their energy is apparent in these works. This effect is probably due to incomplete accounting for the neutron scattering process within the detector when the detector efficiency is calculated by Monte Carlo simulation. This effect is more significant at higher energies. This is an indication of unequal systematic uncertainties. The rationale of this conclusion is based in the analysis performed in Sec. IV C.

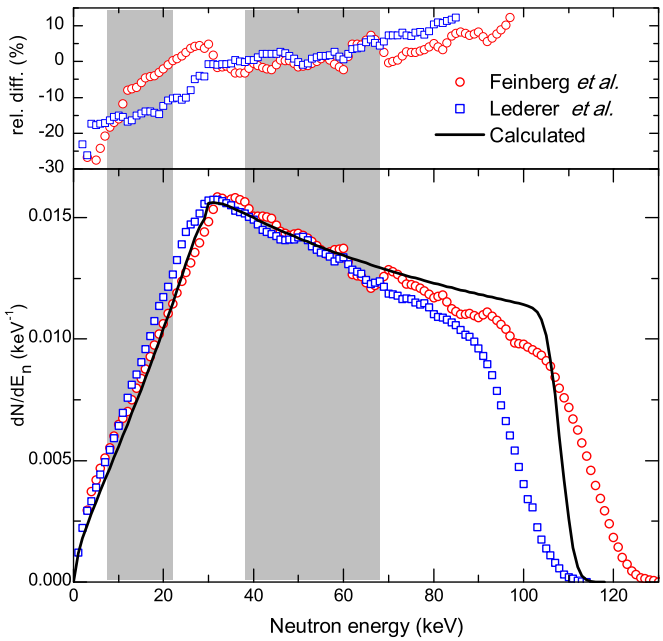


FIG. 12. Neutron spectra from Feinberg *et al.* obtained from Ref. [10] (open circles) and Lederer *et al.* [7] (open squares) both measured at $E_p = 1912$ keV and taken at $0 \pm 3^\circ$ compared to our calculation.

Another remarkable difference between the spectra is the mismatch in the maximum energy which is fixed by the reaction kinematics to a value of $E_n^{\max} = 108.4$ keV for $E_p = 1912$ keV at $\theta = 0^\circ$. Moreover, both experimental spectra exhibit a broaden energy fall compared to the theoretical one. This broadening is due to the instrumentation and must be corrected before using the spectrum. The broadening at the end of the neutron spectrum occurs around a mean value corresponding to the neutron energy equivalent to the mean proton energy entering the Li target. This fact was determined by Monte Carlo simulation of the neutron interaction in our detector. Therefore when proper conversion from TOF to energy spectrum is performed, the minimum of the derivative of the neutron spectrum fall indicates the neutron energy emitted at that angle for the corresponding mean energy of the proton beam.

Performing the neutron energy determination as described above for both spectra we obtain a mean proton energy equal to $1915.7 \pm 0.2$ keV ($E_n^{\max} = 114.4$ keV) for the Feinberg *et al.* spectrum and $1905.9 \pm 0.2$ keV ($E_n^{\max} = 98.1$ keV) for the Lederer *et al.* spectrum. These values differ more than the quoted uncertainties from the reported proton energies. Regarding the spectrum measured by Feinberg *et al.*, where a precise beam energy determination was performed arriving to $1912 \pm 0.5$ keV, the origin of this discrepancy is due, as mentioned by the authors, to a shift in measured energies produced by the iterative procedure used in converting TOF to energy spectrum. Actually, excluding both ends of the neutron spectrum our data compare satisfactorily to Feinberg *et al.*

In the case of the measured spectrum by Lederer *et al.*, based on a comparison with a code which generates neutron spectra, they quoted $1910 \pm 1.2$ keV ($E_n^{\max} = 105.1$ keV). This value yet differs from our determination. This difference also evidences the neutron counting underestimation at high energies and/or a shift in the accelerator energy.

Taking into account that the latter work is claiming to confirm the neutron spectrum measured in Ref. [2] and supporting the absolute capture cross section of gold obtained in that work we calculated the integral spectrum at $E_p = 1912$ keV and performed a comparison to both measurements.

The spectra are plotted in Fig. 13 whereas Table I reproduces integral values of these spectra.

The spectrum-averaged cross section (SACS) is calculated using the $^{197}$Au$(n,\gamma)$ reaction cross section from the ENDF/B-VII.1 [27] library and the percent reproducibility $R$ is calculated, taking Ratynski and Kappeler as reference spectrum, as

$$R = 100\left(1 - \frac{1}{n}\sum_{i=1}^{n}\frac{\left|Y_i^{\text{reference}} - Y_i^{\text{evaluated}}\right|}{Y_i^{\text{reference}}}\right). \quad (9)$$

The same minimization procedure as described in Sec. V for our spectrum is performed to the Ratynski and Kappeler spectrum. The latter was best reproduced by the neutron spectrum generated by a proton beam with $E_p = 1909$ keV.

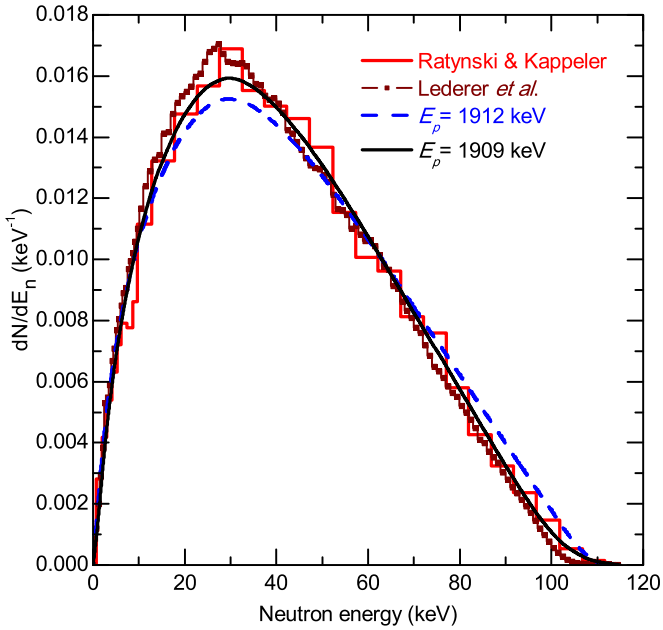


FIG. 13. Angle-integrated neutron spectra from Ratynski and Kappeler [2] (histograms) and from Lederer *et al.* [7] (histogram with centers) and calculated (dashed line) at $E_p = 1912$ keV. Solid line represents the spectrum that best-reproduces Ratynski and Kappeler histogram corresponding to $E_p = 1909$ keV.

This could be an indication of a lower proton energy incident in the Li target than reported.

Apart from the fact that the Lederer *et al.* SACS is 1.9% larger than the Ratynski and Kappeler one, having equal SACS is not an indication of likeness between neutron spectra as suggested in [7]. The spectrum at $E_p = 1912$ keV almost equals Ratynski and Kappeler SACS but reproduces it for 88% while the SACS at $E_p = 1909$ keV differs 1.3% whereas it reproduces the Ratynski and Kappeler spectrum for 95%. The calculated SACS at $E_p = 1912$ keV is in good agreement with the integral cross section value $616 \pm 17$ mb measured by Feinberg *et al.* [8].

TABLE I. $^{197}$Au$(n,\gamma)$ spectrum-averaged cross section (SACS) and reproducibility ($R$) of the spectra represented in Fig. 13.

| Spectrum | SACS (mb) | $R$ (%) |
|---|---|---|
| Ratynski & Kappeler | 627 | 100 |
| Lederer *et al.* | 639 | 85 |
| $E_p = 1912$ keV | 626 | 88 |
| $E_p = 1909$ keV | 619 | 95 |

The calculated SACS using the Ratynski and Kappeler spectrum is 6.5% higher than the $586 \pm 8$ mb measured by them. The first indication of discrepancy is in the quoted uncertainty. The latter only accounted for the measured cross section. When assigning this value to a particular spectrum, in this case the quasistellar spectrum (Fig. 3 in Ref. [2]), the uncertainty due to the neutron spectrum determination plays an important role and could even be higher than that obtained for the cross section value.

According to our results, at least 8 out of the 41 mb difference between the value taken in the activation measurement [2] and Ratynski and Kappeler SACS are probably due to the neutron spectrum uncertainty.

## ACKNOWLEDGMENTS

This work was supported by the Istituto Nazionale di Fisica Nucleare and by the International Atomic Energy Agency (Austria), Contract No. 17883. G. M.-H. is indebted to Laboratori Nazionali di Legnaro staff for is help and support.

[1] H. Beer and F. Kappeler, Phys. Rev. C **21**, 534 (1980).
[2] W. Ratynski and F. Kappeler, Phys. Rev. C **37**, 595 (1988).
[3] D. Petrich, M. Heil, F. Käppeler, J. Kaltenbaek, E.-P. Knaetsch, K. Litfin, D. Roller, W. Seith, R. Stieglitz, F. Voss, and S. Walter, Nucl. Instrum. Methods Phys. Res. A **596**, 269 (2008).
[4] P. Mastinu, G. Martin-Hernandez, and J. Praena, Nucl. Instrum. Methods Phys. Res. A **601**, 333 (2009).
[5] G. Feinberg, M. Paul, A. Arenshtam, D. Berkovits, D. Kijel, A. Nagler, and I. Silverman, Nucl. Phys. A **827**, 590c (2009).
[6] C. Lederer *et al.*, Phys. Rev. C **83**, 034608 (2011).
[7] C. Lederer, F. Kappeler, M. Mosconi, R. Nolte, M. Heil, R. Reifarth, S. Schmidt, I. Dillmann, U. Giesen, A. Mengoni, and A. Wallner, Phys. Rev. C **85**, 055809 (2012).
[8] G. Feinberg, M. Friedman, A. Krasa, A. Shor, Y. Eisen, D. Berkovits, D. Cohen, G. Giorginis, T. Hirsh, M. Paul, A. J. M. Plompen, and E. Tsuk, Phys. Rev. C **85**, 055810 (2012).
[9] G. Martin-Hernandez, P. Mastinu, J. Praena, N. Dzysiuk, R. Capote Noy, and M. Pignatari, Appl. Radiat. Isot. **70**, 1583 (2012).
[10] M. Friedman, D. Cohen, M. Paul, D. Berkovits, Y. Eisen, G. Feinberg, G. Giorginis, S. Halfon, A. Krasa, A. J. M. Plompen, and A. Shor, Nucl. Instrum. Methods Phys. Res. A **698**, 117 (2013).
[11] M. S. Herrera, G. A. Moreno, and A. J. Kreiner, Nucl. Instrum. Methods Phys. Res. B **349**, 64 (2015).
[12] J. P. Theobald, E. Migneco, and C. Cervini, Nucl. Instrum. Methods **95**, 1 (1971).
[13] A. Ritchie, J. Phys. D: Appl. Phys. **9**, 15 (1976).
[14] C. L. Lee and X.-L. Zhou, Nucl. Instrum. Methods Phys Res. B **152**, 1 (1999).
[15] J. F. Ziegler, J. P. Biersack, and M. D. Ziegler, *SRIM—the stopping and range of ions in matter* (SRIM Co., Maryland, 2008).
[16] W. M. Good, J. H. Neiler, and J. H. Gibbons, Phys. Rev. **109**, 926 (1958).
[17] J. B. Marion and J. L. Fowler, *Fast Neutron Physics* (Interscience Publisher, Inc., New York, 1960).
[18] R. L. Macklin and J. H. Gibbons, Phys. Rev. **109**, 105 (1958).

[19] H. Liskien and A. Paulsen, At. Data Nucl. Data Tables **15**, 57 (1975).
[20] G. Audi, A. H. Wapstra, C. Thibault, J. Blachot, and O. Bersillon, Nucl. Phys. A **729**, 337 (2003).
[21] T. Freye, H. Lorenz-Wirzba, B. Cleff, H. P. Trautvetter, and C. Rolfs, Z. Phys. A **281**, 211 (1977).
[22] W. Matysiak, W. V. Prestwich, and S. H. Byun, Nucl. Instrum. Methods Phys. Res. A **643**, 47 (2011).
[23] X-5 Monte Carlo Team, MCNP—A General Monte Carlo N-Particle Transport Code, version 5 (LA-UR-03-1987, 2005).
[24] A. D. Carlson, V. G. Pronyaev, D. L. Smith, N. M. Larson, Chen Zhenpeng, G. M. Hale, F-J. Hambsch, E. V. Gai, Soo-Youl Oh, S. A. Badikov, T. Kawano, H. M. Hofmann, H. Vonach, and S. Tagesen, Nucl. Data Sheets **110**, 3215 (2009).
[25] H. W. Newson, R. M. Williamson, K. W. Jones, J. H. Gibbons, and H. Marshak, Phys. Rev. **108**, 1294 (1957).
[26] K. K. Sekharan, H. Laumer, B. D. Kern, and F. Gabbard, Nucl. Instrum. Methods **133**, 253 (1976).
[27] Evaluated Nuclear Data File [https://www-nds.iaea.org/endf/].